BEHAVIOR AND STRENGTH OF DISTORTIONAL-GLOBAL INTERACTION IN COLD FORMED STEEL LIPPED CHANNEL COLUMNS

João Alfredo de Lazzari
Eduardo de Miranda Batista
joao.lazzari@coc.ufrj.br
batista@coc.ufrj.br
COPPE, Civil Engineering Program, Federal University of Rio de Janeiro
Centro de Tecnologia–Bloco I–Sala I216, Ilha do Fundão, CEP 21945-970, Rio de Janeiro/RJ, Brazil.

Abstract. The cold formed steel members (CFS) are light steel options widely applied in the civil construction. Furthermore, the CFS is a very slender option that allows the buckling behavior to develop on local, distortional and global modes. In this away, it is expected that a greater attention over this structural solution is necessary to guarantee the reliability and safety of the structure. On recent studies, it has been shown that when the local, distortional and global modes occur with similar critical loads, the strength capacity of the structural member is reduced due to a coupled phenomenon. The proposed paper will discuss the distortional-global (D-G) buckling interaction of CFS lipped channels columns under axial load. Additionally, it is developed a computer program (FStr) for elastic buckling analysis, based on Finite Strip Method (FSM), in order to find CFS columns experiencing D-G interaction. The program is developed on MATLAB with an easy graphical user interface. After settled the profiles under strong interaction, a non-linear analysis using Finite Element Method (FEM) is used to find the strength of the columns. Additional analysis and comments are discussed in order to understand the behavior and the strength capacity of the CFS lipped channel columns under the proposed buckling interaction.

Keywords: Cold-formed Steel Lipped Channel Columns; Distortional-Global Buckling Interaction; Finite Strip Method.

1   Introduction

The major tasks of structural engineers are to design low-cost solutions. Thus, saving weight on the structure will lead to solution with less consuming material, and consequently a better economical option. Under these circumstances, light steel construction enables cost saving in the superstructure as well as in the substructure and foundation. Choosing thin-walled steel members is a frequent option because of a less consuming material, engineering design and architectural concepts. However, light gauge steel members are slender structures, which bring up additional stability problems. (Batista *et al.* [1])

The instability phenomena occur commonly on the cold-formed steel (CFS) members, due its very slender thin-walled open cross-sections. In general, these phenomena can be individually named: local – L, distortional – D or global – G (flexural-torsional or flexural) buckling, as can be shown in Fig. 1 in 2D and 3D. More specifically, these general buckling modes can interact resulting in a coupled instability phenomenon. Coupled instabilities are composed by at least two buckling modes and can be identified as L-D, L-G, D-G and L-D-G. According to Batista *et al.* [1], the coupled phenomena lead to erosion of the limit load, in other words means loss of the ultimate strength.
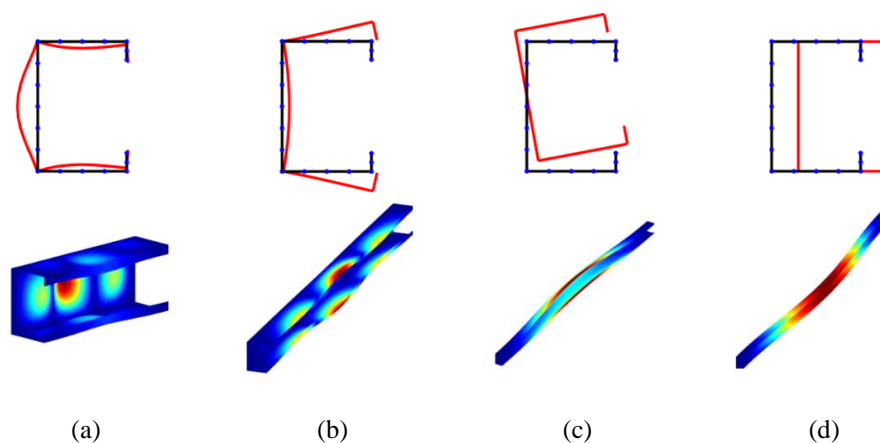
(a)	(b)	(c)	(d)

Figure 1. Cold-formed steel lipped-channel fixed-fixed end condition experiencing (a) local L=252mm, (b) distortional L=1379mm, (c) flexural-torsional L=2557mm and (d) flexural buckling L=14521mm.

So far, the study of the coupled phenomenon on the post-buckling and strength is well known for local-global mode interaction. The L-G interaction is already on the standards for hot-rolled and cold-formed steel members in the effective section method by Batista [2], as well in the direct strength method (DSM) by Schafer [3] & [4]. Initially, the first proposal for the DSM was published by Schafer and Peköz [5], based on the original idea of Hancock *et al.* [6]. Up to now, it is the most adopted method for designing CFS structures.

In addition, the local-distorcional (L-D) interaction has been becoming increasingly popular in the past 20 years. Different studies on the post-buckling and strength on this coupled phenomenon were performed by Yang and Hancock [7], Dinis *et al.* [8], Camotim *et al.* [9], Kwon *et al.* [10], Silvestre *et al.* [11], Martins *et al.* [12] and Matsubara *et al.* [13]. Some of these researches, *e.g.* Yang and Hancock [7], Camotim *et al.* [9], Silvestre *et al.* [11] and Matsubara *et al.* [13], bring about DSM reviews and predictions considering the L-D interaction.

2   DG Interaction Concepts and Relevance

The Distortional-Global (D-G) interaction can be illustrated using the "signature curve", shown in the Fig. 2, the result of the finite strip method program developed by the first author. Basically, when the critical load due the distortional buckling is in a domain relatively close to the global buckling, it is

highly possible to experience the D-G interaction. Figure 2 shows the signature curve for the first and second modes with 10 terms of half-waves and the first mode with only one term of half-wave. In addition, the Fig. 2 present the column's length where it is expected to have the strongest D-G coupled phenomenon. For the signature curve bellow, it is used a lipped channel section C 100x70x15x2.70 mm, under axial compressive load, with fixed-fixed end condition and for a set of 200 lengths, spaced equally in logarithm scale.
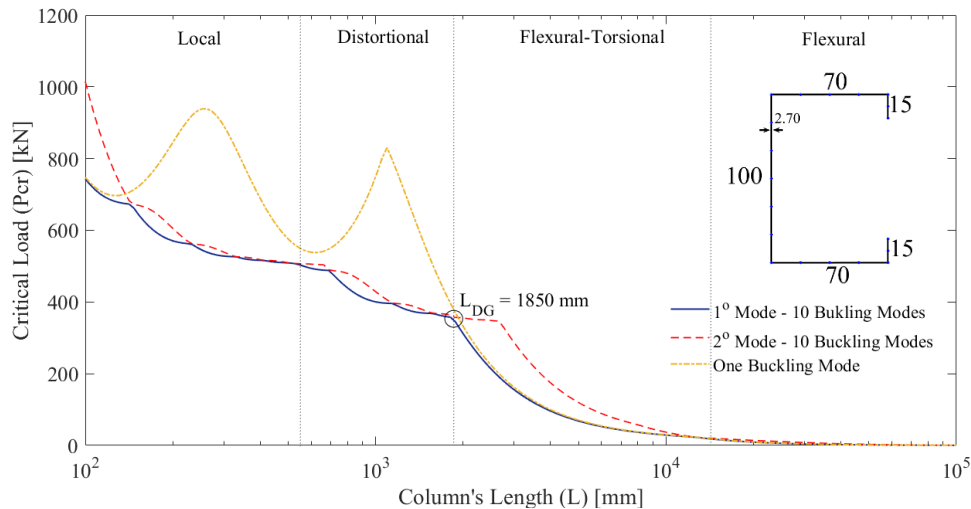

Figure 2. Signature Curve (Critical Load *vs* Column's Length) showing the length of D-G interaction and its elastic buckling modes delimitations.

In the past few years, researches related to the D-G interaction has taken progress. One of the first studies on this topic was discussed by Dinis and Camotim [14] & [15]. These researches performed post-buckling and strength analysis of CFS lipped channels due compressive loads under D-G coupled phenomenon. Rossi *et al.* [16] performed experimental investigations on 48 full-scale tests using stainless steel lipped channel section columns, experiencing distortional, flexural-torsional and combined *distortional-flexural-torsional* buckling mode.

Dinis and Camotim [14] & [15] concluded that in the critical buckling length for D-G interaction, prevails the *distortional-flexural-torsional* mode, as an asymmetrical modal form of the distortional mode. This study contradicts the general concept of exclusively global buckling in that specifically critical buckling length. Also, the authors corroborate that the asymmetrical modal form (*distortional-flexural-torsional*) reduces the post-critic strength, due the instable pos-buckling behavior. In addition, they noticed that the equilibrium path is very sensible to the initial imperfections. Practically, the columns with pure global initial imperfection has a lower critical load than the columns with pure distortional imperfection.

Nonetheless, the North-American standard, AISI S100-12 [17], and the Australian/New Zealand standard, AS/NZS 4600 [18], follows the effective width method, which carry the D-G interaction, according to Dinis and Camotim [15], based on laboratory experiments, conducted by Desmond *et al.* [19]. However, the studies proposed by Desmond *et al.* do not bring an explicit approach for the mechanics of the modal interaction, as it is shown in Dinis and Camotim [15]. Therefore, it is expected that the considerations using in the North-American and Australian/New Zealand standards are conservative.

Recent studies about the D-G interaction were performed on beams in pure bending. Niu *et al.* [20] develop an experimental investigation of stainless steel lipped channels beams. The same authors did a numeric study as a second part of their full study (Niu *et al.* [21]), using the experimental data from the first part. Another study on beams was accomplished by Martins *et al.* [22] & [23], using the generalized beam theory (GBT) as an analysis method. Likewise Niu *et al.* [20] & [21], the study was divided in two parts: Mechanics and Elastic Behavior (Martins *et al.* [22]); Strength, Relevance and DSM Design (Martins *et al.* [23]). Martins *et al.* [24] did the same study, but with zed-sections beams, publish in a

single version.

The newest studies on CFS lipped channel columns, under D-G coupled phenomenon are mostly focused on the mechanics of the D-G interaction and design procedures. Anbarasu [25] performed experimental tests and numeric finite element method, in order to provide a parametric study and design recommendations for the D-G interaction behavior. Martins *et al.* [26] & [27] are recent studies on CFS lipped channel columns, with fixed-fixed end conditions under D-G interaction, which gives design procedures for the direct strength method.

3   The Finite Strip Method

The present work uses the finite strip method (FSM) as an elastic buckling analysis. The FSM was originally formulated by Yau Kai Cheung, honorary professor of The University of Hong Kong (Cheung [28]). On the other hand, it was Gregory J. Hancock, emeritus professor of The University of Sydney, that begum using the method in structural elements as hot-rolled sections and cold-formed steel sections (*e.g.* Hancock *et al.* [29], [30] & [31]). Hancock changed the stiffness matrix of Cheung and developed his own computational program, BFINST (Hancock *et al.* [32]), which gives the solution for the buckling analysis on thin-walled members with open cross sections.

The Finite Strip Method is a particular case of the Finite Element Method (FEM). Briefly, the FEM uses polynomial shape functions in all directions, while the FSM uses polynomials shape functions in transverse direction and trigonometric shape functions in longitudinal direction, which satisfies the boundary conditions. The main advantage in using the FSM is to reduce the structure's degrees of freedom, in order to acquire performance and time in the elastic buckling analysis.

For this investigation, the FSM is implemented in MATLAB platform (MathWorks [33]), and is entitled FStr computer program application. The method formulation is based on the book written by Cheung [28] and other sources: Li and Shafer [34], Schafer [35] and Li [36]. The element is a lower order rectangular strip with two nodal lines (LO2) as can be shown in Fig. 3.
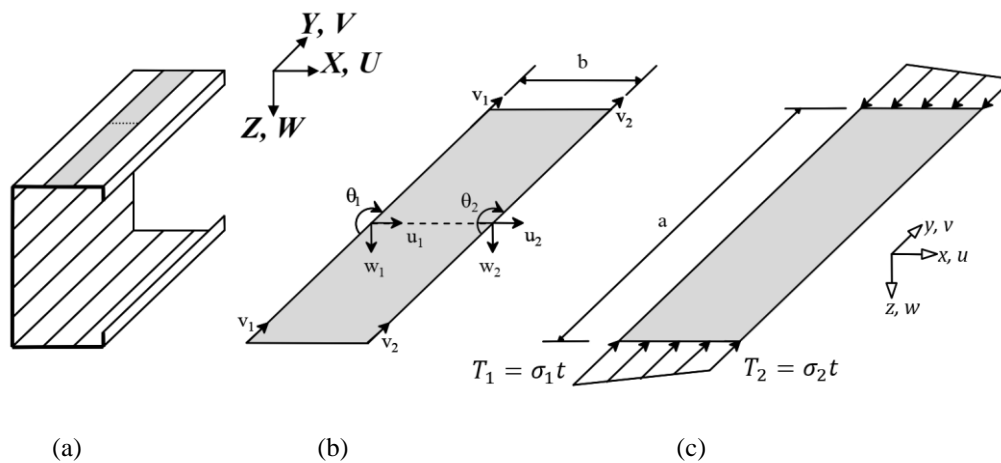

Figure 3. Lower order rectangular strip with two nodal lines (LO2). (a) Strip discretization in a Lipped channel section. (b) Degrees of freedom on nodal lines. (c) External end tractions applied to the strip. Source: Li and Shafer [34].

First, the displacement field inside de strip can be approximated by Eq. (1), using the nodal displacements $\{d\}$, shown in Fig. 3-b, and the shape function matrix $[N]$ (Eq. (2)). The displacements field for each strip, $\{u\ v\ w\}^T$, is determined as a summation of all longitudinal terms, from 1 to m.

$$\begin{Bmatrix} u \\ v \\ w \end{Bmatrix} = [N]\{d\} = \sum_{p=1}^{m}[N]_p\{d\}_p = \sum_{p=1}^{m}[N]_p \{u_1\ v_1\ u_2\ v_2\ w_1\ \theta_1\ w_2\ \theta_2\ \}_p^T. \tag{1}$$

The shape function matrix is given in the Eq. (2). Note that this matrix is composed by polynomial

functions times Y_p, which is a trigonometric function, given in the Eq. (3) for Simple-Simple end condition, and in the Eq. (4) for Fixed-Fixed end condition.

$$[N]_p = \begin{bmatrix} (1-\bar{x})Y_p & 0 & \bar{x}\,Y_p & 0 & 0 & 0 & 0 & 0 \\ 0 & (1-\bar{x})\frac{Y_p'}{\lambda_p} & 0 & \bar{x}\frac{Y_p'}{\lambda_p} & 0 & 0 & 0 & 0 \\ 0 & 0 & 0 & 0 & (1-3\bar{x}^2+2\bar{x}^3)Y_p & x(1-2\bar{x}+\bar{x}^2)Y_p & (3\bar{x}^2-2\bar{x}^3)Y_p & x(\bar{x}^2-\bar{x})Y_p \end{bmatrix}. \tag{2}$$

$$Y_p = sin(\lambda_p\, y). \tag{3}$$

$$Y_p = sin(\lambda_p\, y)\, sin\left(\frac{\pi y}{a}\right). \tag{4}$$

In Eqs. (2) to (4) $\lambda_p = p\pi/a$, $\bar{x} = x/b$ and p is de half-wave term. More end conditions can be found in Li and Schafer [34].

The formulation of the finite strip now can be defined using the principle of minimum total energy. According to Cheung [28], the principles states that "*of all compatible displacements satisfying given boundary conditions, those which satisfy the equilibrium conditions make the total potential energy assume a stationary value*". In another words, the Eq. (5) shows in mathematical form

$$\left\{\frac{\partial\Pi}{\partial\{d\}}\right\} = \left\{\frac{\partial\Pi}{\partial\{d\}_1}\quad\frac{\partial\Pi}{\partial\{d\}_2}\quad\cdots\quad\frac{\partial\Pi}{\partial\{d\}_m}\right\}^T = \{0\},\ where\ \Pi = U + W \tag{5}$$

in which Π is the total potential energy, U is the strain energy and W is the potential energy of external forces.

By definition, the strain energy of a three dimensional solid is defined by Eq. (6).

$$U = \frac{1}{2}\oiiint \{\varepsilon\}^T\{\sigma\}\,dV = \frac{1}{2}\oiiint\{d\}^T[B]^T[D][B]\{d\}\,dV. \tag{6}$$

In Eq. (6) $\{\varepsilon\}$ is the strain, compound by the sum of the bending and twisting curvature strain ($\{\varepsilon_B\}$) with the normal and shear strain ($\{\varepsilon_M\}$). Also, $\{\sigma\}$ is the stress, related to the strains, $[B]$ is the strain-displacement matrix and $[D]$ is the elasticity matrix.

The stiffness matrix can now be computed substituting Eq. (6) in the Eq. (5). Doing the appropriate differentiation and organizing in the form $[k]\{d\} - \{F\} = \{0\}$, the general stiffness matrix is given by:

$$[k] = \oiiint[B]^T[D][B]\,dV = \sum_{i=1}^{s}\sum_{j=1}^{s}\sum_{p=1}^{m}\sum_{q=1}^{n}\int_0^t\int_0^a\int_0^b[B^i]_p^T[D][B^j]_q\,dx\,dy\,dz. \tag{7}$$

Solving Eq. (7) for the membrane strain, which consider plane stress assumptions, it leads to the elastic stiffness matrix for the membrane, given by Eq. (8). The matrix corresponds to the half-waves p and q, from node i to node j.

$$[k_M^{ij}]_{pq} = t\begin{bmatrix} \left(\frac{E_1I_1}{b}+\frac{G_{xy}bI_5}{3}\right) & \left(-\frac{E_2\nu_xI_3}{2\lambda_q}-\frac{G_{xy}I_5}{2\lambda_q}\right) & \left(-\frac{E_1I_1}{b}+\frac{G_{xy}bI_5}{6}\right) & \left(-\frac{E_2\nu_xI_3}{2\lambda_q}+\frac{G_{xy}I_5}{2\lambda_q}\right) \\ \left(-\frac{E_2\nu_xI_2}{2\lambda_p}-\frac{G_{xy}I_5}{2\lambda_p}\right) & \left(\frac{E_2bI_4}{3\lambda_p\lambda_q}+\frac{G_{xy}I_5}{b\lambda_p\lambda_q}\right) & \left(\frac{E_2\nu_xI_2}{2\lambda_p}-\frac{G_{xy}I_5}{2\lambda_p}\right) & \left(\frac{E_2bI_4}{6\lambda_p\lambda_q}-\frac{G_{xy}I_5}{b\lambda_p\lambda_q}\right) \\ \left(-\frac{E_1I_1}{b}+\frac{G_{xy}bI_5}{6}\right) & \left(\frac{E_2\nu_xI_3}{2\lambda_q}-\frac{G_{xy}I_5}{2\lambda_q}\right) & \left(\frac{E_1I_1}{b}+\frac{G_{xy}bI_5}{3}\right) & \left(\frac{E_2\nu_xI_3}{2\lambda_q}+\frac{G_{xy}I_5}{2\lambda_q}\right) \\ \left(-\frac{E_2\nu_xI_2}{2\lambda_p}+\frac{G_{xy}I_5}{2\lambda_p}\right) & \left(\frac{E_2bI_4}{6\lambda_p\lambda_q}-\frac{G_{xy}I_5}{b\lambda_p\lambda_q}\right) & \left(\frac{E_2\nu_xI_2}{2\lambda_p}+\frac{G_{xy}I_5}{2\lambda_p}\right) & \left(\frac{E_2bI_4}{3\lambda_p\lambda_q}+\frac{G_{xy}I_5}{b\lambda_p\lambda_q}\right) \end{bmatrix}. \tag{8}$$

Where: $\lambda_p = \frac{p\pi}{a}$; $\lambda_q = \frac{q\pi}{a}$; $I_1 = \int_0^a Y_pY_q dy$; $I_2 = \int_0^a Y_p'Y_q'dy$; $I_3 = \int_0^a Y_pY_q''dy$; $I_4 = \int_0^a Y_p''Y_q''dy$; $I_5 = \int_0^a Y_p''Y_q dy$;

$E_1 = \frac{E_x}{1-\nu_x\nu_y}$; $E_2 = \frac{E_y}{1-\nu_x\nu_y}$; $G_{xy} = \frac{E_xE_y}{E_x(1+2\nu_y)+E_y}$.

The integrals I_1, I_2, I_3, I_4 and I_5 are analytically solved in Li and Schafer [34]. Moreover, E_x and E_y are the elastic modulus for x and y directions, ν_x and ν_y are the Poisson's ratio for x and y directions and G_{xy} is the shear modulus.

Solving Eq. (7) for the bending strain, which consider Kirchoff thin plate theory assumptions, it leads to the elastic stiffness matrix for the bending, given by Eq. (9).

$$[k_{B1}^{ij}]_{pq} = 840 \, D_x I_1 \begin{bmatrix} 6 & 3b & -6 & 3b \\ 3b & 2b^2 & -3b & b^2 \\ -6 & -3b & 6 & -3b \\ 3b & b^2 & -3b & 2b^2 \end{bmatrix} ; \quad [k_{B2}^{ij}]_{pq} = 14 \, D_1 b^2 \begin{bmatrix} -36I_2 & -33bI_2 & 36I_2 & -3bI_2 \\ -33bI_3 & -4b^2I_2 & 3bI_2 & b^2I_2 \\ 36I_2 & 3bI_2 & -36I_2 & 33bI_2 \\ -3bI_2 & b^2I_2 & 33bI_3 & -4b^2I_2 \end{bmatrix} ;$$

$$[k_{B3}^{ij}]_{pq} = 14 \, D_1 b^2 \begin{bmatrix} -36I_3 & -3bI_3 & 36I_3 & -3bI_3 \\ -3bI_2 & -4b^2I_3 & 3bI_3 & b^2I_3 \\ 36I_3 & 3bI_3 & -36I_3 & 3bI_3 \\ -3bI_3 & b^2I_3 & 3bI_2 & -4b^2I_3 \end{bmatrix} ; \quad [k_{B4}^{ij}]_{pq} = D_y \, b^4 I_4 \begin{bmatrix} 156 & 22b & 54 & -13b \\ 22b & 4b^2 & 13b & -3b^2 \\ 54 & 13b & 156 & -22b \\ -13b & -3b^2 & -22b & 4b^2 \end{bmatrix} ;$$

$$[k_{B5}^{ij}]_{pq} = 56 \, D_{xy} \, b^2 I_5 \begin{bmatrix} 36 & 3b & -36 & 3b \\ 3b & 4b^2 & -3b & -b^2 \\ -36 & -3b & 36 & -3b \\ 3b & -b^2 & -3b & 4b^2 \end{bmatrix} ;$$

$$[k_B^{ij}]_{pq} = \frac{1}{420 \, b^3} \left([k_{B1}^{ij}]_{pq} + [k_{B2}^{ij}]_{pq} + [k_{B3}^{ij}]_{pq} + [k_{B4}^{ij}]_{pq} + [k_{B5}^{ij}]_{pq} \right). \tag{9}$$

In Eq. (9) $I_1 = \int_0^a Y_p Y_q \, dy$; $I_2 = \int_0^a Y_p' Y_q' \, dy$; $I_3 = \int_0^a Y_p Y_q'' \, dy$; $I_4 = \int_0^a Y_p'' Y_q'' \, dy$; $I_5 = \int_0^a Y_p'' Y_q \, dy$;

$D_x = \frac{E_x t^3}{12(1 - \nu_x \nu_y)}$; $D_y = \frac{E_y t^3}{12(1 - \nu_x \nu_y)}$; $D_1 = \frac{\nu_x E_y t^3}{12(1 - \nu_x \nu_y)} = \frac{\nu_y E_y t^3}{12(1 - \nu_x \nu_y)}$; $D_{xy} = \frac{G_{xy} t^3}{12}$; $G_{xy} = \frac{E_x E_y}{E_x(1 + 2\nu_y) + E_y}$.

The integrals I_1, I_2, I_3, I_4 and I_5 are analytically solved in Li and Schafer [34].

For the stability problem, it is necessary formulate the geometric matrix due an initial stress. The finite strip element is LO2, subjected to initial tractions that varies linearly, as shown in Fig. 3-c. However, the distribution of edge tractions along the longitudinal axis is constant. Thus, the potential energy due the in-plane forces is given by:

$$V = \frac{1}{2} \oiiint \{\sigma_1 - (\sigma_1 - \sigma_2)\bar{x}\} \left\{ \left(\frac{\partial u}{\partial y}\right)^2 + \left(\frac{\partial v}{\partial y}\right)^2 + \left(\frac{\partial w}{\partial y}\right)^2 \right\} dV \quad sendo, \bar{x} = \frac{x}{b}. \tag{10}$$

Working on the Eq. (10) using matrix formulation, it leads to a more organized expression, in function of the loadings T_1 and T_2, reaching to the Eq. (11).

$$V = \frac{1}{2} \int_0^a \int_0^b \{T_1 - (T_1 - T_2)\bar{x}\} \{d\}_m^T [G]_m^T [G]_n \{d\}_n \, dx \, dy = \frac{1}{2} \sum_{p=1}^m \sum_{q=1}^n \{d\}_p^T [kg]_{pq} \{d\}_q . \tag{11}$$

The geometric matrix can also be obtained with the minimization of the total potential energy due the initial stress. But it is already obvious to notice that geometric matrix formulation in the expression inside the total potential energy, Eq. (11). The general expression for the geometric stiffness matrix or the initial stress matrix is written in Eq. (12).

$$[kg] = \sum_{i=1}^s \sum_{j=1}^s \sum_{p=1}^m \sum_{q=1}^n \int_0^a \int_0^b \{T_1^i - (T_1^i - T_2^j)\bar{x}\} [G^i]_p^T [G^j]_q \, dx \, dy. \tag{12}$$

Similar to the stiffness matrix, the initial stress matrix will be divided into membrane and bending. Solving the Eq. (12) for the membrane case, it leads to geometric stiffness matrix for the membrane, shown in Eq. (13).

$$[kg_M^{ij}]_{pq} = \frac{b}{12} \begin{bmatrix} (3T_1 + T_2)I_5 & 0 & (T_1 + T_2)I_5 & 0 \\ 0 & \frac{(3T_1 + T_2)I_4}{\lambda_p \lambda_q} & 0 & \frac{(T_1 + T_2)I_4}{\lambda_p \lambda_q} \\ (T_1 + T_2)I_5 & 0 & (T_1 + 3T_2)I_5 & 0 \\ 0 & \frac{(T_1 + T_2)I_4}{\lambda_p \lambda_q} & 0 & \frac{(T_1 + 3T_2)I_4}{\lambda_p \lambda_q} \end{bmatrix}. \tag{13}$$

In Eq. (13) we have $\lambda_p = \frac{p\pi}{a}$; $\lambda_q = \frac{q\pi}{a}$; $T_1 = \sigma_1 t$; $T_2 = \sigma_2 t$; $I_4 = \int_0^a Y_p'' Y_q'' \, dy$; $I_5 = \int_0^a Y_p'' Y_q \, dy$.

Likewise, solving the Eq. (12) for the bending case, it leads to geometric stiffness matrix for the bending, shown in Eq. (14).

$$\left[kg_B^{ij}\right]_{pq} = \frac{bI_5}{35}\begin{bmatrix} (10T_1 + 3T_2) & \frac{(15T_1+7T_2)b}{12} & \frac{9(T_1+T_2)}{4} & -\frac{(7T_1+6T_2)b}{12} \\ \frac{(15T_1+7T_2)b}{12} & \frac{(5T_1+3T_2)b^2}{24} & \frac{(6T_1+7T_2)b}{12} & -\frac{(T_1+T_2)b^2}{8} \\ \frac{9(T_1+T_2)}{4} & \frac{(6T_1+7T_2)b}{12} & (3T_1 + 10T_2) & -\frac{(7T_1+15T_2)b}{12} \\ -\frac{(7T_1+6T_2)b}{12} & -\frac{(T_1+T_2)b^2}{8} & -\frac{(7T_1+15T_2)b}{12} & \frac{(3T_1+5T_2)b^2}{24} \end{bmatrix}. \tag{14}$$

Where: $T_1 = \sigma_1 t$; $T_2 = \sigma_2 t$; $I_5 = \int_0^a Y_p'' Y_q dy$.

For the assumed flat shell strip used (LO2), there is no interaction between the bending and the membrane. Due to that, the elastic stiffness matrix and the geometric stiffness matrix is obtained assembling the membrane and bending matrices through a simple combination, as described in Eq. (15).

$$\left[k^{ij}\right]_{pq} = \begin{bmatrix} \left[k_M^{ij}\right]_{pq} & [0]_{4\times4} \\ [0]_{4\times4} & \left[k_B^{ij}\right]_{pq} \end{bmatrix}_{8\times8} \qquad \left[kg^{ij}\right]_{pq} = \begin{bmatrix} \left[kg_M^{ij}\right]_{pq} & [0]_{4\times4} \\ [0]_{4\times4} & \left[kg_B^{ij}\right]_{pq} \end{bmatrix}_{8\times8}. \tag{15}$$

The matrices in the Eq. (15) are for the half-waves p and q, from node i to node j, in local coordinates. Thus, the global matrices are obtained assembling all the half-waves terms in each corresponding degree of freedom. For the assembling, it is necessary to transform the local coordinate into global coordinates. In this case, it is considered a common y axis for the local and global coordinates. More details about the assembly of the global stiffness matrices can be found in Schafer and Ádány [37].

After the assembling, the general stability solution is obtained solving the eigenvalue equation described in the Eq. (16).

$$([K] - [\Lambda][KG])[\Phi] = [0] \quad or \quad [K][\Phi] = [\Lambda][KG][\Phi]. \tag{16}$$

Using the global elastic stiffness matrix $[K]$, the global geometric stiffness matrix $[KG]$ and a proper eigenvalue problem solver, it is possible to obtain the eigenvalues $[\Lambda]$, which are the critical tractions, and the eigenvectors $[\Phi]$, which are the critical modal shapes.

4 Computer Program FStr

The finite strip method is implemented in MATLAB platform, MathWorks [33], which turn out to be a computer program application. Entitle FStr, the program performs an elastic buckling analysis of thin walled structures. A graphical user interface (GUI) of the program is designed, in order to make the program a useful and easy tool to perform the buckling analysis (Fig. 4).

4.1 Graphical User Interface

The GUI is created using the App Designer, from MathWorks, which is a powerful and easy development environment for designing apps. The FStr computer program and its GUI design is inspired on the CUFSM 5 – Finite Strip Elastic Buckling Analysis Application – by Schafer *et al.* [37], [38], [39] & [40]. Figure 4 shows the GUI of the FStr computer program.

Basically, the computer program is in function of some initial parameters and Fig. 4 shows in details those parameters. It is necessary to discretize the section in nodal points, to increase more precision on the method. The panel *Coordinates* has: the node number, coordinate in global X and Z direction and the initial stress in each node. The *Elements* panel represents the connectivity between the nodes, in order to define the element and also its width. Also, the panel *Material* has the elastic modulus and the Poisson's ratio for x and y local directions. The panel with the *Strip Properties* is defined the boundary condition, terms of half-waves and lengths of the thin-walled structural element. After all the initial parameters defined, the program is set up to perform the analysis. As a result of the analysis, the signature curve is shown, in addition to the 2D modal shape in each length and in a specific length position ratio. Also, it can be plotted a 3D modal shape for a specific length, with a color scale, showing
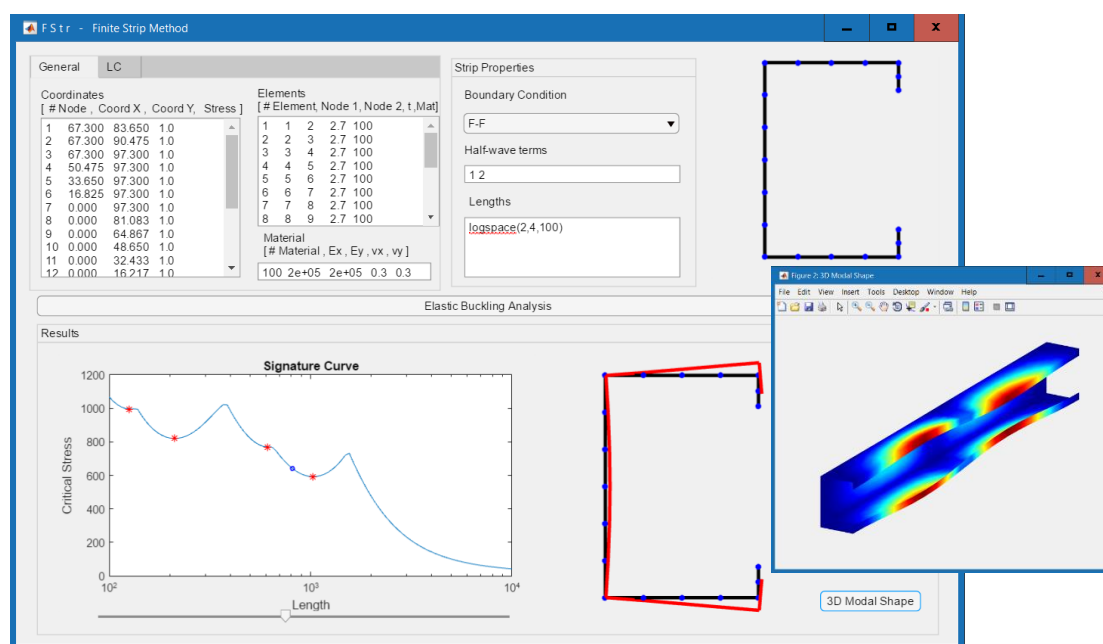
the resultant displacement.

Figure 4. The FStr Graphical User Interface.

The program implementation was planned to have a better performance than the others elastic buckling analysis programs, with an easy and light GUI. As a result of that, the program has a powerful role on optimization problems, which turned out to reduce the time for running the objective function.

4.2   Validation of the FStr Program

The FStr computer program is validated comparing its results with other methods and computer applications. The methods used for comparison are the Finite Element Method (FEM), Generalized Beam Theory (GBT) and Constrained and Unconstrained Finite Strip Method (CUFSM).

For the validation, it is performed an elastic buckling analysis for a range of 200 lengths of columns. Also, for all the methods used, it is treated a column under uniform axial compression, with fixed-fixed end condition,

The FEM is used with assistance of the ANSYS Mechanical APDL 17.0 [41]. The main mode extraction method to be used for the buckling analysis is the subspace iteration, which is suitable to find the modes for large models. Additional finite element model specifications about the column discretization, type of element, boundary conditions, etc. is well detailed in section 5.

The other method used for comparison, the GBT, is used with accordance to the GBTUL 2.0.4.4 computer application, by Bebiano *et al.* [42]. For this method, it is used all the conventional modes, numerical solution with 20 beam finite elements, with clamped-clamped end condition.

Lastly, the CUFSM is a method based on the FSM, which is also the same method as it was used for the developed computer application program, FStr. The CUFSM, by Schafer *et al.* [37], [38], [39] & [40], is an open free source program created by the professor Ben Schafer's thin-walled structures research group at Johns Hopkins University. For this method, it is used the same initial parameters as used in the FStr program: 10 half-wave terms, clamped-clamped end condition and 18 strips.

The graph of critical load versus column's length is illustrated in the Fig. 5 in accordance with the relative difference between the FStr computer application program with other numerical solutions.
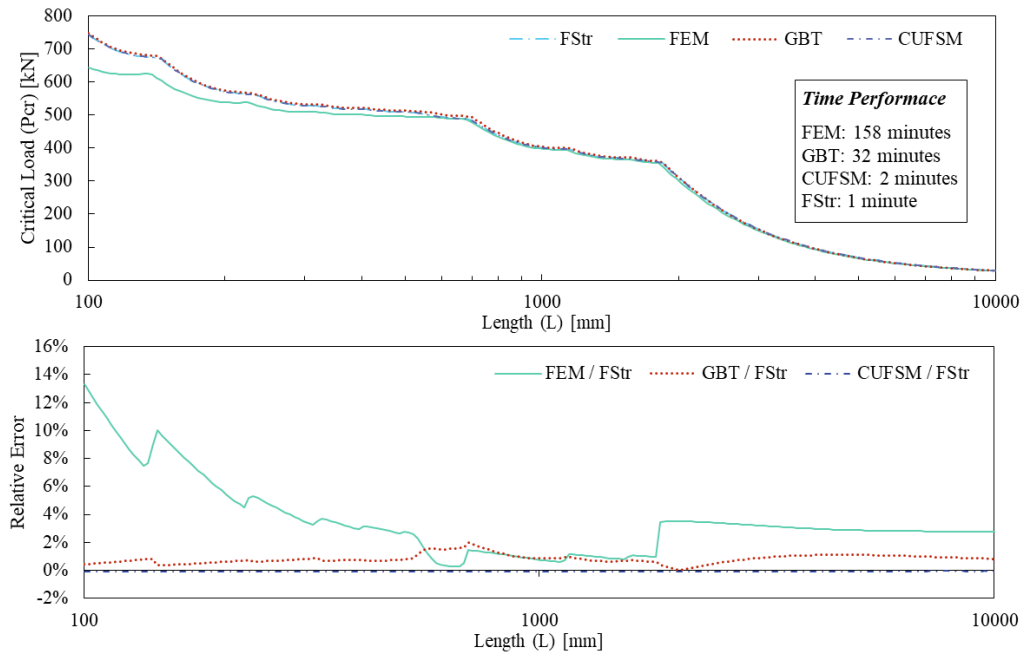
Figure 5. Signature Curve and Relative Difference for validation of the FStr computer application program.

First, comparing the two graphs in the Fig. 5, it can be seen that the CUFSM and the FStr provides the same results, with a maximum difference of 0.000056%. Also, the FStr reached close to the GBT method, with a maximum relative error of 2.0%. However, comparing the FStr with the FEM, the maximum relative error is 13.3%, which can be seen clearly in the signature curve. On the other hand, this maximum error occurs in short column's length, which for this research is irrelevant. As shown in Fig. 2, the D-G modal interaction is stronger near to the length 1850mm. For a certain length range near to L=1850mm, the maximum relative difference is around 3.51%, which is an acceptable error or difference between the FEM and FSM.

With respect to the modal shape, the Fig. 6 and 7 shows the comparison of the buckling mode shape for the column's length of 1722 mm and 2222 mm, respectively. Note that the FStr gives the same buckling mode with same maximum amplitude, as it is given by the FEM.
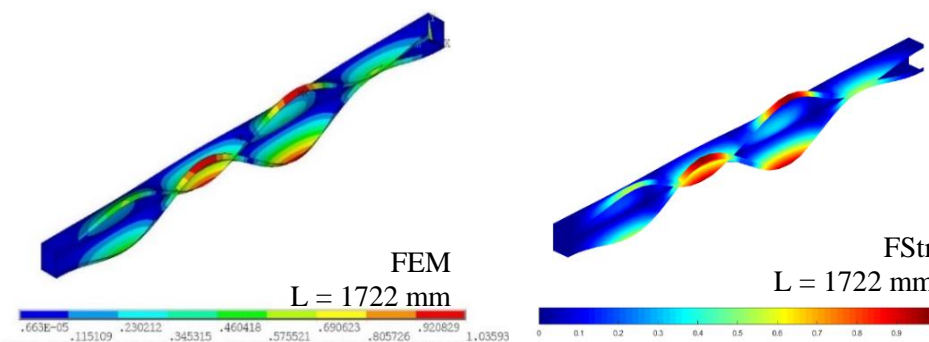

Figure 6. Tridimensional modal shapes comparison between FEM and FStr at L=1722 mm.

Further, the time of performance of each method is shown in Fig. 5. Note that the FStr is the faster method, with a great precision, compared to the other methods. Accordingly, the FStr computer program application, is a powerful tool for elastic buckling analysis, that can be used for optimizzation problems or large number of buckling analysis.
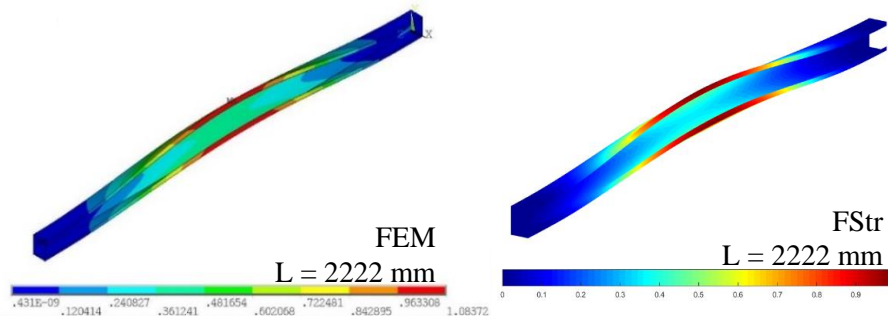
FEM
L = 2222 mm

FStr
L = 2222 mm

Figure 7. Tridimensional modal shapes comparison between FEM and FStr at L=2222 mm.

5 Finite Element Modeling

For a numerical investigation of the D-G interaction, a FEM is performed in order to understand the structural behavior. Also, the FEM is used with assistance of ANSYS Mechanical APDL 17.0 [41]. The analysis using the FEM is addressed to detect the strength of the structural element, using a shell finite element analysis.

5.1 Modeling Specifications

First, the material properties are defined as a linear constant, for a homogeneous and isotropic steel. For the elastic modulus it is defined 200 GPa and the major Poisson's ratio equal 0.3. Also, the material is considered as a bilinear isotropic hardening, which uses the von Mises yield criteria with an isotropic work hardening presumption. This hardening assumption, consider that the initial slope of the strain-stress curve is the elastic modulus with a tangent modulus equal to zero, in the plastic strain. The yield strength of the material is 345 MPa, and with a thickness of 2.70mm. The base plate uses the same material property but with a 12mm of thickness.

Secondly, the finite element type using here is the SHELL281. According to the ANSYS Theory Reference [41], the SHELL281 has 8 nodes, with 6 degrees of freedom, and is appropriate for linear, large rotation and large strain nonlinear situations. In addition, the SHELL281 formulation is placed on logarithmic strain and true stress measures. For this research, the finite element option is an element stiffness with bending and membrane considerations.

Thirdly, the geometry and imperfections of the column is created using an FSM analysis previously. The FStr program performs the elastic buckling analysis, and with the corresponded modal critical shape, it generates points that are inserted into an APDL as KEYPOINTS. The modal critical shape is inserted as an initial imperfection, with an maximum amplitude depending on the mode (L/1000 for global imperfection and 0.94t for distortional imperfection, according with Schafer and Pekoz [43]). In this case, the shell geometry is composed by non-planar surfaces, when connecting 4 nearby KEYPOINTS. Figure 8 shows the point generation with predefined imperfections.

The mesh generation has a particularity, it generates quadrilateral and triangle-shaped elements with an element size of 5mm. This mixed mesh occurs due the predefined imperfections from the FStr program. Even though the element shape chosen for the whole column was quadrilateral-shaped, it might emerge triangle-shaped elements, when the mesh is generated. This happens because the areas generation for the mesh are formed by non-planar surfaces. This is the reason why in this research it is used SHELL218 instead of SHELL181, which has less nodes and degrees of freedom, as well as the SHELL281 gives more reliable results for triangular elements, while SHELL181 is not recommend for triangular-shaped elements. Figure 8 shows the mesh generation from the areas.

With respect to the boundary conditions, the column has fixed-fixed end condition. For this type of model, it requires specific constraints. Both extremities of the column have constraints on displacements in *x* and *y* direction, and constraints on rotation in *x*, *y* and *z* direction (see Fig. 8). Another constraint in necessary in the middle of the column, in a node in the middle of web, which prevent displacement in z

direction. This additional constraint in the middle of the columns is needed to avoid free body translation. The constraints in the extremity of the column can be seen in the Fig. 8.
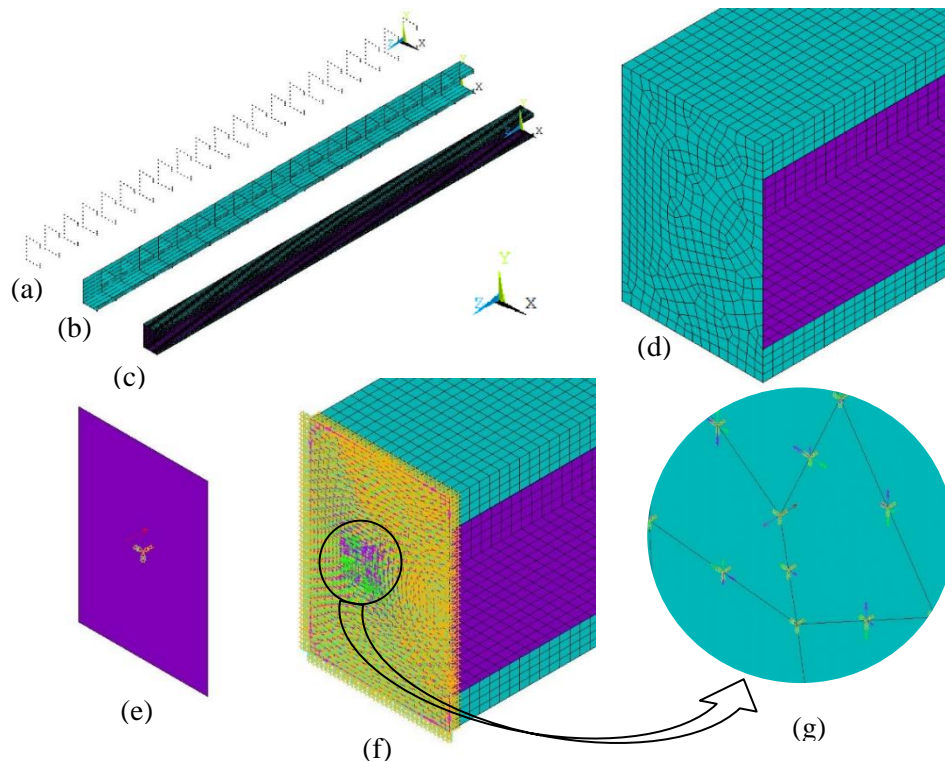

Figure 8. Finite Element Model generation in ANSYS Mechanical APDL 17.0. (a) KEYPOINT generation with the initial imperfection, (b) four-point areas generated connecting KEYPOINTS, (c) mesh generation on the areas, (d) mesh at plate on end condition, (e) end boundary constrains and punctual concentrated load applied to the area on the extremities, (f) all the constrains applied on each element at the ends of the column and (g) zoom of the punctual concentrated load applied to the elements.

Lastly, the compressive load is applied at the ends of the column. The external load is applied as a punctual concentrated load in the centroid of the section, at both ends.

After all the model defined, the non-linear analysis can be executed based on the Newton-Raphson procedure, using the arc-length method or also commonly called "The modified Riks method". This method is convenient for solutions of unstable problems that has a nonlinear static equilibrium.

5.2   Validation of Finite Element Model

Since this research aims the D-G interaction, the finite element model is validated for columns that experienced only global buckling mode and distortional buckling mode, before collapsing. For the validation, it is used experimental results from Heva [44], Salles [45] and Matsubara *et al.* [13].

Global Buckling Mode Validation: The global buckling validation is performed using columns tested by Heva [44]. This author has performed lab tests of multiple columns under different temperatures developing the flexural-torsional buckling. For the present research, only the results for the specimen with room temperature (20°C) are considered. Table 1 shows all the parameters and results of the numerical and lab tests performed by Heva [44], and also the results obtained in the present research. Also, Table 1 has all the measured geometries of the specimen, the material properties given by standard tensile tests and the actual specimen imperfections. For results, Table 1 bring forward the ultimate strength for 3 cases: strength using FEM by Heva [44], strength using lab tests performed by Heva [44] and strength using FEM given by the present investigation.

Table 1. Ultimate strength results of specimens from Heva [44], both numerical and lab tests, and the numerical results obtained in the present research.

Column	Measured Geometry					fy	E	Impref.	Ultimate Strength		
									Heva, 2009		Author's
	t	b_W	b_f	b_s	L				$P_{U\,TEST}$	$P_{U\,FEM}$	$P_{U\,FEM}$
[#]	[mm]	[mm]	[mm]	[mm]	[mm]	[MPa]	[N/mm2]		[kN]	[kN]	[kN]
G250-1.95-1800	1.95	74.82	50.06	14.87	1740	271	188000	L/2558	87.94	90.70	93.59
G450-1.90-1800	1.88	74.67	49.94	14.51	1740	515	206000	L/2949	120.42	129.00	127.60
G550-0.95-1800	0.95	54.94	34.88	8.00	1740	615	205000	L/2485	24.72	25.40	25.71

Notice that the author's numerical ultimate strength is similar to the numerical model and lab tests given by Heva [44]. The proposed numerical model has a relative error of 6.3%, 6.0% and 4.0% regarding with lab test of Heva [44] and 3.2%, -1.1% and 1.2% differences regarding with the numerical solution of Heva [44], respectively for the models G250-1.95-1800, G450-1.90-1800 and G550-0.95-1800.

For more convincing results, the graphs load *versus* displacement of the middle top flange at mid span for the 3 column specimens are shown in Fig. 9 and Fig. 10. These graphs show the displacement behavior of a specific point during the loading procedure.

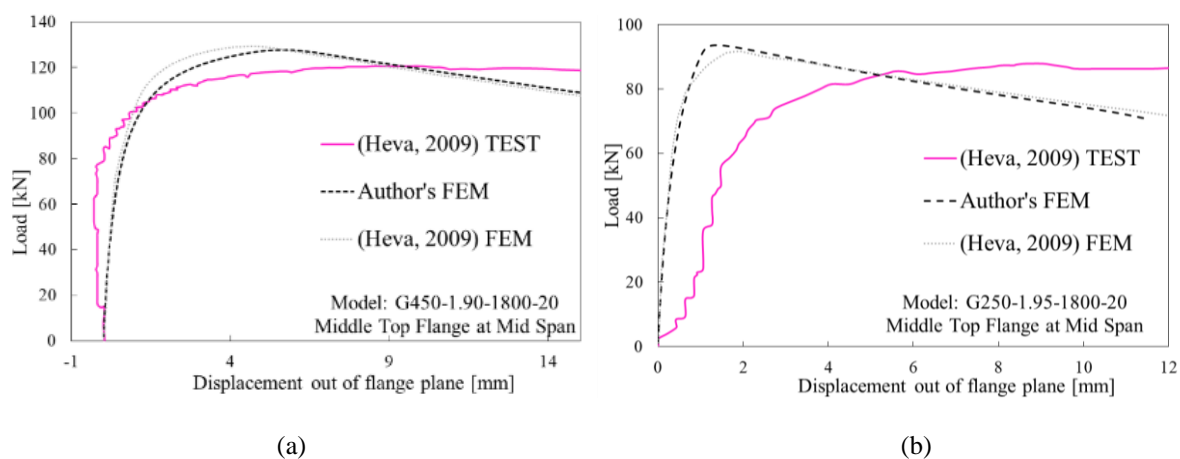(a)   (b)

Figure 9. Load versus displacement of the middle top flange at mid span of (a) G250-1.95-1800, (b) G450-1.90-1800.
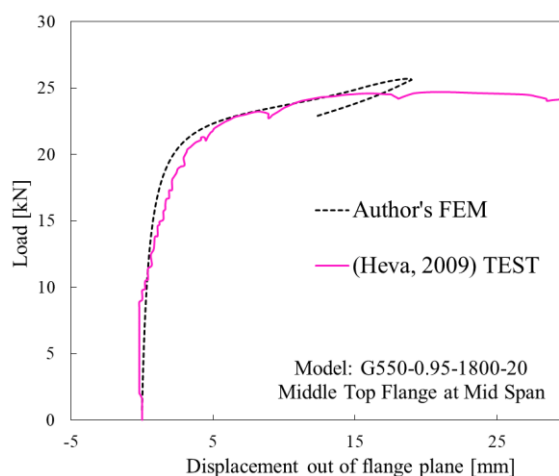

Figure 10. Load versus displacement of the middle top flange at mid span of G550-0.95-1800.

Note in Fig. 10 that the author's FEM have a similar stability path as Heva's [44] test. On the other hand, in Fig. 9(b), the lab tests are kindly translated on the displacement direction. However, the numerical model performed in this research has a very close behavior to the numerical model performed by Heva [44]. The obtained results allow concluding that the developed finite element model is validated for flexural-torsional buckling analysis.

Distortional Buckling Mode Validation: The validation is performed using a column tested by Salles [45]. Updated information about the tested column is in Matsubara, Batista and Salles [13]. The column cross-section geometry is shown in the Fig. 11-a. The lipped channel CFS column specimen was 2529 millimeters long, with material properties of 342 MPa of yield strength and 179.468 GPa of elastic modulus (quite low Young modulus extracted from standard tensile tests). The testing was performed at the COPPE Laboratory of Structures and Materials Professor Lobo Carneiro (LabEST). As a result, the specimen reached its experimental ultimate strength of 33.4 kN, while the FEM modeled in this research, lead to an ultimate strength of 35.3 kN, taking $0.1t$ amplitude of the distortional buckling mode initial geometrical imperfection. Figure 11-a shows a comparison of the stability path of the web extremities at mid span, for the laboratory experiment and the FEM solution.
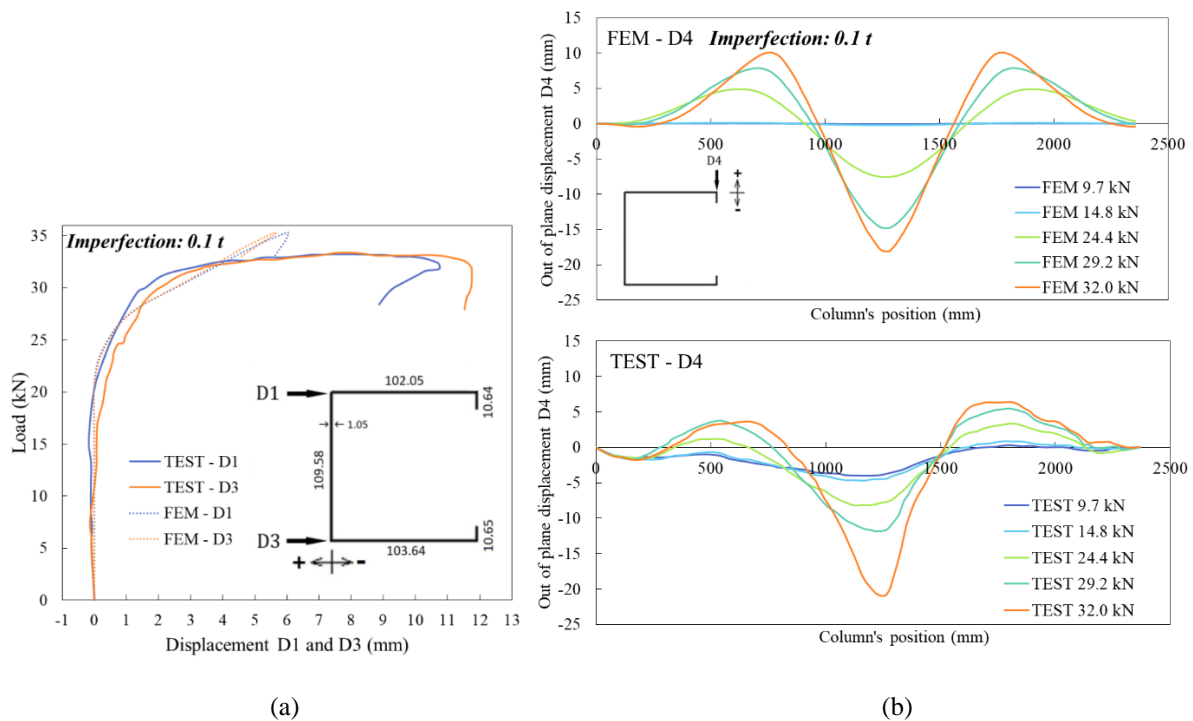

Figure 11. (a) Displacement D4 along the column's position, with 5 load increments; (b) Load versus displacement of the web extremities at mid span of LC specimen by Salles [45].

Note in Fig. 11-a that the stability path of the FEM is pretty close to the lab experiment for small displacements. For larger displacements, the FEM model tends to behave into a linear path until it collapses, while the laboratory test shows a long plateau before collapse.

Figure 11-b, shows the flange displacement out of plane D4, along the column's position for 5 loading steps.

Observe that the same behavior of distortional buckling is clearly shown in the FEM and in the experimental test, with 3 half-waves of distortional modal shape. In addition, the buckling behavior is increased with the load increment, until it collapses.

6   Study of Initial Imperfections on DG Interaction

As shown in Figure 2, the D-G interaction occurs more intensely in a specific length (L=1850 mm). For the same CFS member (LC 100x70x15x2.70 mm) and conditions, as done in the elastic buckling solution given by Fig 2, a FEM analysis is performed in order to understand the behavior and strength of the column, when subjected to different combinations of distortional and global initial imperfections. The goal of this study is to identify how sensitive the column is to initial geometrical imperfection using modal combination.

6.1   Modal Combination

The requirement of combining the modal shapes shown up due its difficulty to find a D-G interaction in the elastic buckling analysis for the initial imperfection mode. As one can see in Fig. 2, the derivative of the signature curve before L=1850 mm and after this length, changes drastically, as well as the modal shape and modal participation. In this case, it is hard to get a shape that presents a clearly D-G interaction. Because of this obstacle of getting a D-G interaction shape mode, the first and second modes are combined.

The modal combination is performed using the first and the second mode shapes, for a length of 1850mm. The buckling odes, in 2D and 3D shape, and the modal participation of the first and second modes are illustrated in Fig. 12. The critical load and the shapes were given by the computer application FStr, however, the modal participation percentages were given by the CUFSM computer program.
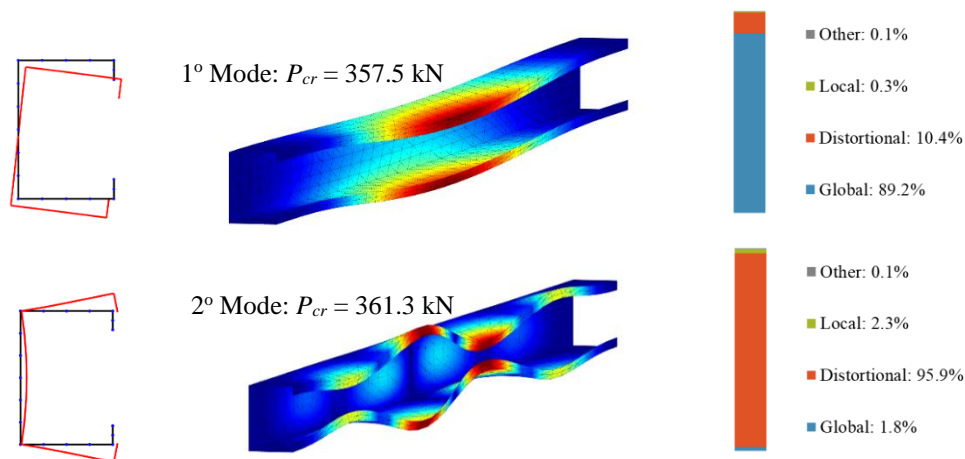

Figure 12. Modal shapes of 1° and 2° modes and its modal participation, for LC 100x70x15x2.70 at L=1850mm.

The modal combination is carried out using the displacement field obtained in the finite strip method (Eq. (1)), and combining linearly the first and second mode displacements. Equation (17) shows the linear combination of the displacements. These displacements are obtained from the eigenvectors $[\Phi]$, given by the eigenvalue equation, Eq. (16). The matrix of the critical modal shapes $[\Phi]$ represents the nodal line displacements for the degrees of freedom shown in Fig. 3-b for each mode. This means that each column of the matrix $[\Phi]$ represents the critical modal shape for one mode. In order to obtain the displacement field on any point inside each strip, Eq. (1) performs the linear transformation from the nodal line solution to the displacement field, with assistance of the shape function matrix [N], Eq. (2).

$$\begin{Bmatrix} u \\ v \\ w \end{Bmatrix} = \beta_1 \begin{Bmatrix} u \\ v \\ w \end{Bmatrix}_{Mode\ 1} + \beta_2 \begin{Bmatrix} u \\ v \\ w \end{Bmatrix}_{Mode\ 2}. \tag{17}$$

Since the displacement field is normalized, with maximum displacement of 1, the coefficients β_1 and β_2 are the parameters of amplification of these shapes. These parameters are defined in Eq. (18), where $C_1 = \cos(\theta)$, $C_2 = \sin(\theta)$, θ is an angle for changing the modal combination, and A is the maximum amplitude for initial imperfection.

$$\beta_1 = \frac{C_1}{|C_1|+|C_2|} A_1, \ \ \beta_2 = \frac{C_2}{|C_1|+|C_2|} A_2. \tag{18}$$

Note that Eq. (18) shows a combination of the maximum amplitude for the initial imperfection. When $\theta = 0^\circ$, then, $\beta_1 = A_1$ and $\beta_2 = 0$, on the other hand, when $\theta = 90^\circ$, then, $\beta_1 = 0$ and $\beta_2 = A_2$. Basically, the parameter θ is a single parameter that allows changing the initial imperfections and consequently the modal combination shape. In this research, the first mode is the flexural-torsional with 89.2% of global participation and the second mode is the distortional with 95.9% of modal participation (Figure 12). Due to that, for the first mode it is used $A_1 = L/1000$ and for the second mode $A_2 = 0.94 \, t$. These amplitudes for the geometrical imperfections where used based on Martins *et al.* [27] and Schafer and Pekoz [43]. Figure 13 shows the column with the initial imperfections combined, amplified by 10 times, for θ varying from 0° to 90°, with 15° of incremental steps, for 3D shape and θ varying from 0° to 180°, also by 15° of increment, for 2D shape.
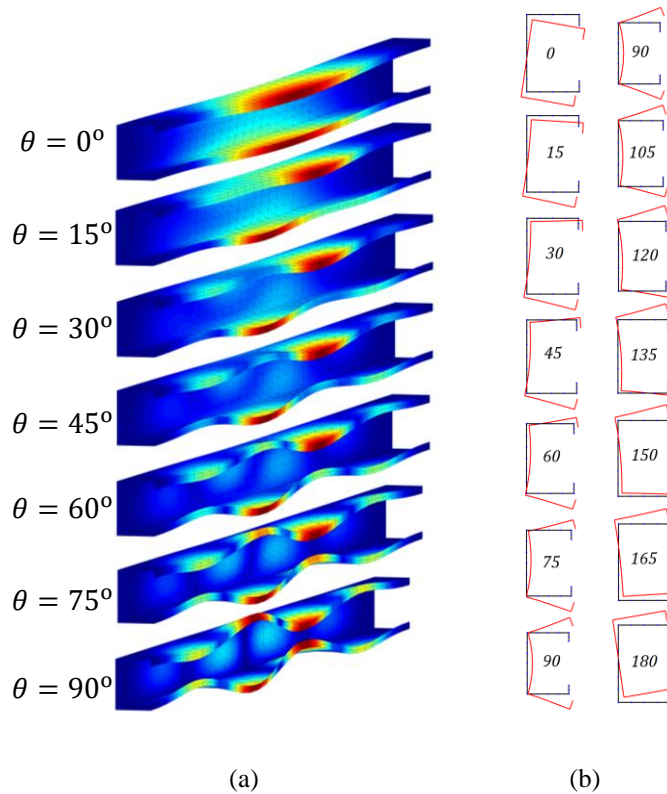

(a)   (b)

Figure 13. Modal shapes combining first and second mode: (a) 3D modal shapes from $\theta = 0^\circ$ to 90° and (b) 2D modal shapes at 40% of the maximum length from $\theta = 0^\circ$ to 180°.

Note that varying the angle θ, it changes the contribution of each mode in the initial imperfections. Also, observe that varying θ from 0° to 90° it has a symmetric modal combination as varying from 90° to 180°, as is shown in figure 13.

Varying the angle θ from 0° to 345°, by 15° of incremental steps, it is possible to generate 24 columns with different types of distortional and global modal shapes combination. From that, the columns are performed on FEM software ANSYS, in order to understand the buckling and strength behavior. The ultimate strength of the columns, are exposed in Table 2, as well as the percentage of the mode's contribution to the initial imperfection.

Table 2 shows the mode contribution changes from 100% to -100% for each mode, but with a total modulus summation of 100%. Basically, the negative percentage of the mode represents a combination of the mode in opposite modal shape. In this way, it is possible to combine all the possible cases. With respect to the ultimate strength capacity, note that it did not change too much. However, it is important to point out how this strength changes over the θ variation. To see clearly this deviation, Fig. 14 shows two graphs of this variation, in cartesian coordinate (Fig. 14-a) and polar coordinate (Fig. 14-b).

Table 2. Ultimate strength of columns with different modes combination, from $\theta = 0^\circ$ to 345° under D-G modal interaction.

| Theta | MODE* | Beta (Ampl. Imperfei.) | | % Mode 1 | % Mode 2 | Ultimate Strength |
| | | Mode 1 | Mode 2 | | | |
[Degrees]				[%]	[%]	[kN]
0	G (+)	1.85	0.00	100%	0%	205.59
15	DG (+)	1.46	0.54	79%	21%	205.15
30	DG (+)	1.17	0.93	63%	37%	203.39
45	DG (+)	0.93	1.27	50%	50%	202.70
60	DG (+)	0.68	1.61	37%	63%	202.69
75	DG (+)	0.39	2.00	21%	79%	202.50
90	D (+)	0.00	2.54	0%	100%	200.59
105	DG (-)	-0.39	2.00	-21%	79%	202.50
120	DG (-)	-0.68	1.61	-37%	63%	202.69
135	DG (-)	-0.93	1.27	-50%	50%	202.70
150	DG (-)	-1.17	0.93	-63%	37%	203.39
165	DG (-)	-1.46	0.54	-79%	21%	205.15
180	G (-)	-1.85	0.00	-100%	0%	205.59
195	DG (+)	-1.46	-0.54	-79%	-21%	205.15
210	DG (+)	-1.17	-0.93	-63%	-37%	203.39
225	DG (+)	-0.93	-1.27	-50%	-50%	202.70
240	DG (+)	-0.68	-1.61	-37%	-63%	202.69
255	DG (+)	-0.39	-2.00	-21%	-79%	202.50
270	D (-)	0.00	-2.54	0%	-100%	200.59
285	DG (-)	0.39	-2.00	21%	-79%	202.50
300	DG (-)	0.68	-1.61	37%	-63%	202.69
315	DG (-)	0.93	-1.27	50%	-50%	202.70
330	DG (-)	1.17	-0.93	63%	-37%	203.39
345	DG (-)	1.46	-0.54	79%	-21%	205.15

* Modal shape of the initial imperfection, where (+) is the modal shape in original form and (-) is the modal shape multiplied by -1.
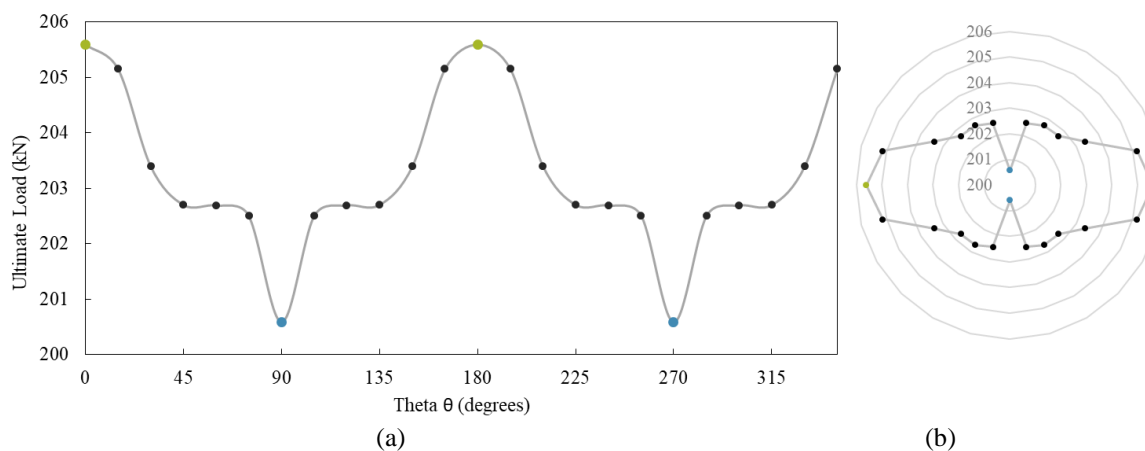

(a)

(b)

Figure 14. Ultimate load strength versus the angle θ - of modal shape combination - for (a) cartesian system and (b) polar system.

Figure 14-a shows clearly a cyclic behavior of the strength. Also, in Fig. 14-b it can be seen the symmetry of the behavior in the first quadrant (0º to 90º). Basically, from $\theta = 0º$ to 180º, the behavior is the same as $\theta = 180º$ to 360º, which is obvious to notice by Table 2.

The cyclic behavior of the strength can be seen from another perspective. From that, Fig. 15 illustrates the FEM models deformed shapes at the limit load (column strength) step. For this case, it is shown only the columns with $\theta = 0º, 45º, 90º, 135º, 180º, 225º, 270º, 315º$ and 360º.
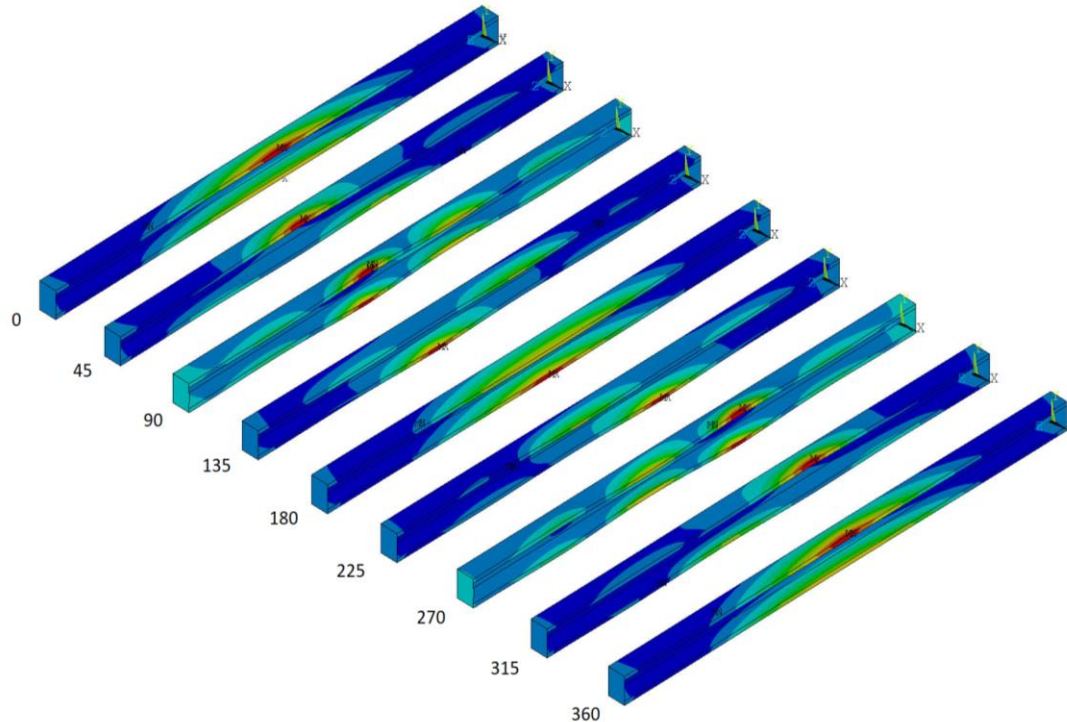

Figure 15. Maximum vector displacement at the limit load (or column strength) step for $\theta = 0º$ to 360º, incremented by 45º.

Note by Fig. 15 that the maximum displacement changes based on the initial imperfection shape. This shows how sensitive the column behaves depending on the initial imperfection shape. Also, it can be seen a cyclic behavior of the maximum displacement, from a global failure to a distortional one. The maximum displacement cycle starts at mid span at the top flange and moves to the nearest distortional maximum half-wave deformation (around 40% of the maximum length). From that, the maximum displacement "jumps" to the bottom flange, with a distortional collapse. From that point, the maximum displacement moves to the mid span again, but at the bottom flange and, after that, the cycle repeats. Those modal shape on ultimate strength step shows that an analysis from $\theta = 0º$ to 90º is already enough to perform a D-G interaction investigation.

Another interesting result is related to the maximum absolute displacement. The 50% of mode 1 and mode 2 combination ($\theta = 45º, 135º, 225º$ and 315º) has the maximum absolute displacement of 7.2 mm, while the four columns with the lowest absolute displacement are with the pure mode 1 ($\theta = 0º$ and 360º) and pure mode 2 ($\theta = 90º$ and 270º), with 4.5mm and 5.7mm respectively.

7   Conclusion and Future Work

This paper presented a buckling behavior analysis of cold-formed steel lipped channel columns under D-G interaction. It has shown that a few researches have taking progress in the last 15 years. Due to that, it is important to explored this coupled phenomenon that is not well known.

The first progress of the present investigation, come with the development of the FStr computer

program application. This finite strip method program has shown a very good accuracy in comparison with the most popular programs. The CUFSM provides pretty much the same result, with a maximum error of 0.000056%. Also, the FStr reached close to the GBT method, with a maximum relative difference of 2.0%. Last but not least, the FEM has shown a maximum relative difference of 3.51%, for a certain length range near to L=1850mm, which is the length of D-G mode interaction of the adopted CFS lipped channel member. In addition, the FStr has demonstrated the same buckling modal shape as the FEM. Regarding with the time of performance, the FStr program has present 158 times faster than the FEM, 32 times faster than the GBT and 2 times faster than the CUFSM, for the initial parameters and terms of half-waves considered. To sum up, the FStr program represents, without a doubt, an elastic buckling analysis and is the faster solution for the present case, with a great accuracy if compared to the other computer programs.

The validation of the finite element method for the CFS thin-walled column strength determination, has shown that the model specifications are in accordance with the available laboratory experiments. The structural analysis with the finite element SHELL281, combined with the initial geometrical imperfections generated from the FStr, has demonstrated satisfactory behavior for global and distortional buckling analysis and the column strength identification. This allows conclude that the finite element model analysis is validated for the conditions adopted in the research.

The study of modal combination of initial imperfection on D-G interaction, has also provided useful information. First, using a single parameter θ, it was able to vary the mode combination in an effortless way. Also, it has been shown that varying θ on the unit circle leaded to a cyclic and symmetric strength behavior. This conclusion can also be seen in the deformed shape on the ultimate load step, showing a cyclic and symmetric form. To sum up, varying $\theta = 0º$ to $90º$ is already enough to perform a deeper D-G interaction investigation. However, it is important to analyze the stability path on post-buckling in specific points to have a more robust conclusion about the symmetric deformed shape behavior.

Future proposals for this research are focused on laboratory testing of some columns experiencing the D-G coupled phenomenon. The laboratory experiments are a good opportunity to better understand the behavior and to perform a future direct strength method designing procedure concerning the D-G modal interaction. Also, some additional recommendations on this research are related to the implementation of the modal participation in the FStr computer program application, in order to separate the modal forms, which can be useful for initial imperfections generation of pure modes.

Acknowledgements

References

[1] M. Pignataro, V. Gioncu, G.C. Ruta, E. de M. Batista, R. Casciaro, Z. Gaspar, Phenomenological and Mathematical Modelling of Structural Instabilities, SpringerWien New York, 2005.
[2] E. de M. Batista, Effective section method: A general direct method for the design of steel cold-formed members under local-global buckling interaction, Thin-Walled Struct. 48 (2010) 345–356. doi:10.1016/j.tws.2009.11.003.
[3] B. Schafer, Direct Strength Method (DSM) Design Guide, in: Committee on Specifications for the Design of Cold-Formed Steel Structural Members (Ed.), Des. Guid. CFXX-X, Am. Iron Steel Inst., American Iron and Steel Institute, 2006. https://www.ce.jhu.edu/cfs/.
[4] B.W. Schafer, Review: The Direct Strength Method of cold-formed steel member design, J. Constr. Steel Res. 64 (2008) 766–778. doi:10.1016/j.jcsr.2008.01.022.
[5] B.W. Schafer, T. Peköz, Direct Strength Prediction of Cold-Formed Steel Members Using Numerical Elastic Buckling Solutions, in: 14th Int. Spec. Conf. Cold-Formed Steel Struct., St. Louis, 1998: pp. 69–76.

[6] G.J. Hancock, Y.B. Kwon, E. Stefan Bernard, Strength design curves for thin-walled sections undergoing distortional buckling, J. Constr. Steel Res. 31 (1994) 169–186. doi:10.1016/0143-974X(94)90009-4.

[7] D. Yang, G.J. Hancock, Compression Tests of High Strength Steel Channel Columns with Interaction between Local and Distortional Buckling, J. Struct. Eng. (2004). doi:10.1061/(asce)0733-9445(2004)130:12(1954).

[8] D. Camotim, P. Borges Dinis, N. Silvestre, FEM-based analysis of the local-plate/distortional mode interaction in cold-formed steel lipped channel columns, Comput. Struct. 85 (2007) 1461–1474. doi:10.1016/j.compstruc.2007.02.013.

[9] D. Camotim, N. Silvestre, P.B. Dinis, Direct strength prediction of lipped channel columns experiencing local-plate/distortional interaction, Adv. Steel Constr. 5 (2009) 49–71.

[10] Y.B. Kwon, B.S. Kim, G.J. Hancock, Compression tests of high strength cold-formed steel channels with buckling interaction, J. Constr. Steel Res. (2009). doi:10.1016/j.jcsr.2008.07.005.

[11] N. Silvestre, D. Camotim, P.B. Dinis, Post-buckling behaviour and direct strength design of lipped channel columns experiencing local / distortional interaction, JCSR. 73 (2012) 12–30. doi:10.1016/j.jcsr.2012.01.005.

[12] A.D. Martins, P.B. Dinis, D. Camotim, P. Providencia, Interacção local-distorcional em colunas de aço enformadas a frio com secção em C reforçada na alma, in: Congr. Métodos Numéricos Em Eng., APMTAC, Lisboa, Portugal, 2015: p. 20.

[13] G.Y. Matsubara, E. de M. Batista, G.C. Salles, Lipped channel cold-formed steel columns under local-distortional buckling mode interaction, Thin-Walled Struct. 137 (2019) 251–270. doi:10.1016/j.tws.2018.12.041.

[14] P.B. Dinis, Camotim D., Post-buckling behavior and strength of cold-formed steel lipped channel columns affected by distortional/global mode interaction, in: Struct. Stab. Res. Counc. Stab. Conf., Nashville, TN, 2008: pp. 405–431.

[15] P.B. Dinis, D. Camotim, Post-buckling behaviour and strength of cold-formed steel lipped channel columns experiencing distortional/global interaction, Comput. Struct. 89 (2011) 422–434. doi:10.1016/j.compstruc.2010.11.015.

[16] B. Rossi, J.-P. Jaspart, K.J.R. Rasmussen, Combined Distortional and Overall Flexural-Torsional Buckling of Cold-Formed Stainless Steel Sections: Experimental Investigations, J. Struct. Eng. 136 (2010) 354–360. doi:10.1061/(asce)st.1943-541x.0000147.

[17] AISI S100-12, North American Specification for the Design of Cold-Formed Steel Structural Members, American Iron and Steel Institute, 2012.

[18] AS/NZS 4600, Cold-formed steel structures, Standards Australia & Standard New Zealand, Australian/New Zealand StandardTM, 2018.

[19] T.P. Desmond, T. Peköz, G. Winter, Edge Stiffeners for Cold-formed Steel Members, Int. Spec. Conf. Cold-Formed Steel Struct. (1978) 38.

[20] S. Niu, K.J.R. Rasmussen, F. Fan, Distortional–global interaction buckling of stainless steel C-beams: Part I — Experimental investigation, J. Constr. Steel Res. 96 (2014) 127–139. doi:10.1061/(asce)st.1943-541x.0001137.

[21] S. Niu, K.J.R. Rasmussen, F. Fan, Distortional–global interaction buckling of stainless steel C-beams: Part II — Numerical study and design, J. Constr. Steel Res. Distortional–Global. 96 (2014) 40–53. doi:10.1061/(asce)st.1943-541x.0001131.

[22] A.D. Martins, D. Camotim, R. Gonçalves, P.B. Dinis, 07.02: Distortional-global interaction in lipped channel beams: Part I: Mechanics and elastic behaviour, Ce/Papers. 1 (2017) 1493–1502. doi:10.1002/cepa.192.

[23] A.D. Martins, D. Camotim, P.B. Dinis, 07.03: Distortional-global interaction in lipped channel beams: Part II: Strength, relevance and DSM design, Ce/Papers. 1 (2017) 1503–1512. doi:10.1002/cepa.193.

[24] A.D. Martins, D. Camotim, P.B. Dinis, Distortional-global interaction in lipped channel and zed-section beams: Strength, relevance and DSM design, Thin-Walled Struct. (2018). doi:10.1016/j.tws.2018.02.015.

[25] M. Anbarasu, Influence on ultimate strength of Cold- Formed Steel Lipped Channel Columns subjected to Interaction on Distortional- Global Buckling, Adv. Nat. Appl. Sci. 8 (2017) 192–201.

[26] A.D. Martins, D. Camotim, R. Goncalves, P.B. Dinis, Mechanics of the local-distortional interaction in fixed-ended lipped channel columns, in: Proc. Int. Colloq. Stab. Ductility Steel Struct. SDSS 2016, 2016: pp. 1–22.

[27] A.D. Martins, D. Camotim, P.B. Dinis, On the distortional-global interaction in cold-formed steel columns: Relevance, post-buckling behaviour, strength and DSM design, J. Constr. Steel Res. 145 (2018) 449–470. doi:10.1016/j.jcsr.2018.02.031.

[28] Y.K. Cheung, Finite Strip Method in Structural Analysis, Pergamon Press, Adelaide, 1976. doi:10.1016/0898-1221(77)90078-5.

[29] G.J. Hancock, Local, Distortional, and Lateral Buckling of I-Beams, J. Struct. Div. 104 (1978) 1787–1798. https://cedb.asce.org/CEDBsearch/record.jsp?dockey=0008405.

[30] G.J. Hancock, N.S. Trahair, M.A. Bradford, Web Distortion and Flexural-Torsional Buckling, J. Struct. Div. 106 (1980) 1557–1571. https://cedb.asce.org/CEDBsearch/record.jsp?dockey=0009600.

[31] G.J. Hancock, Interaction Buckling in I-Section Columns, J. Struct. Div. 107 (1981) 165–179. https://cedb.asce.org/CEDBsearch/record.jsp?dockey=0009979.

[32] G. Hancock, T. Murray, D. Ellifritt, Cold-Formed Steel Structures to the AISI Specification, 2001. doi:10.1201/9780203907986.

[33] MathWorks, MATLAB Using MATLAB Graphics, Matlab. (2000).

[34] Z. Li, B. Schafer, FSM stability solutions for general boundary conditions and extension of cFSM, in: Twelfth Int. Conf. Civil, Struct. Environ. Eng. Comput., Madeira, Portugal, 2009. doi:10.4203/csets.22.5.

[35] B.W. Schafer, Chapter 2: Elastic Buckling Solution Methods for Cold-formed Steel Elements and Members, Ph.D. Thesis, Cornell University, 1998.

[36] Z. Li, Buckling Analysis of the Finite Strip Method and Theoretical Extension of the Constrained Finite Strip Method for General Boundary Conditions., Research Report, Baltimore, MD, 2009. http://www.ce.jhu.edu/bschafer.

[37] S. Ádany, B.W. Schafer, Buckling analysis of cold-formed steel members using CUFSM: Conventional and constrained finite strip methods, in: 18th Int. Spec. Conf. Cold-Formed Steel Struct., 2006. doi:10.1016/j.tws.2006.03.013.

[38] B.W. Schafer, Cold-formed steel behavior and design: analytical and numerical modeling of elements and members with longitudinal stiffeners, PhD dissertation, Cornell University, Ithaca, NY, 1997.

[39] Z. Li, B.W. Schafer, Buckling analysis of cold-formed steel members with general boundary conditions using CUFSM: Conventional and constrained finite strip methods, in: Int. Spec. Conf. Cold-Formed Steel Struct., 2010. doi:10.1016/j.tws.2006.03.013.

[40] B.W. Schafer, CUFSM: elastic buckling analysis of thin-walled members by finite strip analysis, (2018). https://www.ce.jhu.edu/bschafer/cufsm/.

[41] ANSYS Inc., ANSYS Mechanical APDL Theory Reference, ANSYS Inc. (2013). doi:www.ansys.com.

[42] R. Bebiano, N. Silvestre, D. Camotim, GBTUL - A code for the buckling analysis of cold-formed steel members, 19th Int. Spec. Conf. Recent Res. Dev. Cold-Formed Steel Des. Constr. (2008).

[43] B.W. Schafer, T. Pekoz, Computational modeling of cold-formed steel : characterizing geometric imperfections and residual stresses, J. Constr. Steel Res. 47. 47 (1998) 193–210. doi:0143-974X/98/$19.00.

[44] Y.B. Heva, Behaviour and design of cold- formed steel compression members at elevated temperatures, Thesis, School of Urban Developments Queensland University of Technology, 2009.

[45] G.C. de Salles, Investigação Analítica, Numérica e Experimental do Modo de Flambagem Distorcional em Perfis Formados a Frio, Dissertação de Mestrado, Universidade Federal do Rio de Janeiro, COPPE, 2017.